Tailored magnetoelastic sensor geometry for advanced functionality in wireless biliary stent monitoring systems

2010 J. Micromech. Microeng. 20 075040

(http://iopscience.iop.org/0960-1317/20/7/075040)

IOP PUBLISHING JOURNAL OF MICROMECHANICS AND MICROENGINEERING

J. Micromech. Microeng. **20** (2010) 075040 (13pp) doi:10.1088/0960-1317/20/7/075040

Tailored magnetoelastic sensor geometry for advanced functionality in wireless biliary stent monitoring systems

Scott R Green[1,3] **and Yogesh B Gianchandani**[1,2]

[1] Department of Mechanical Engineering, 1301 Beal Ave., University of Michigan, Ann Arbor, MI 48109, USA
[2] Department of Electrical Engineering and Computer Science, 1301 Beal Ave., University of Michigan, Ann Arbor, MI 48109, USA

E-mail: greensr@umich.edu

Received 8 January 2010, in final form 22 April 2010
Published 28 June 2010
Online at stacks.iop.org/JMM/20/075040

Abstract
This paper presents three types of wireless magnetoelastic resonant sensors with specific functionalities for monitoring sludge accumulation within biliary stents. The first design uses a geometry with a repeated cell shape that provides two well-separated resonant mode shapes and associated frequencies to permit spatial localization of mass loading. The second design implements a pattern with specific variation in feature densities to improve sensitivity to mass loading. The third design uses narrow ribbons joined by flexible couplers; this design adopts the advantages in flexibility and expandability of the other designs while maintaining the robust longitudinal mode shapes of a ribbon-shaped sensor. The sensors are batch patterned using photochemical machining from 25 μm thick 2605SA1 Metglas^{TM}, an amorphous Fe–Si alloy. Accumulation of biliary sludge is simulated with paraffin or gelatin, and the effects of viscous bile are simulated with a range of silicone fluids. Results from the first design show that the location of mass loads can be resolved within ~5 mm along the length of the sensor. The second design offers twice the sensitivity to mass loads (3000–36 000 ppm mg^{-1}) of other designs. The third design provides a wide range of loading (sensitive to at least 10× the mass of the sensor) and survives compression into a 2 mm diameter tube as would be required for catheter-based delivery.

(Some figures in this article are in colour only in the electronic version)

1. Introduction

Stents are tubular structures used to impart and maintain patency in a variety of vessels and ducts that have become constricted as a result of stenotic pathology. Though the act of implanting a stent relieves symptoms caused by the constriction, in-stent restenosis—a reappearance of the narrowing, typically due to the reaction of the body to the presence of the stent—is a risk associated with all stenting procedures. An example of a stent application area—and the focus of this work—is the bile duct. Restenosis can occur in an unpredictable time frame of 2–12 months via formation of a bacterial matrix on and around the stent known as biliary 'sludge' [1, 2]. This sludge accumulates and eventually leads to occlusion of the duct and a reappearance of symptoms related to blockage, including jaundice, pruritus and liver malfunction.

Current techniques for diagnosing a blockage use a blood test to monitor enzymes such as bilirubin and alkaline phosphatase, among others. Imaging of the duct—using either computed tomography or endoscopic cholangiography—then confirms the presence of a blockage [3]. Because enzyme levels may not increase until after the blockage is significant, this approach can result in either unnecessary, pre-scheduled interventions, or in untimely interventions after patients exhibit outward symptoms of blockage. As such, a direct

---

[3] Author to whom any correspondence should be addressed.

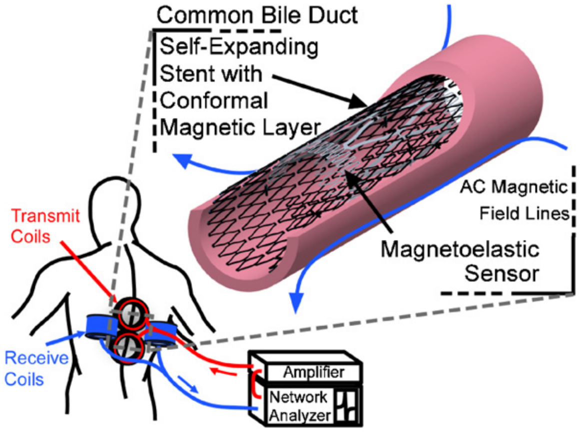

Figure 1. Conceptual diagram of *in vivo* magnetoelastic sensing of sludge accumulation for biliary stents. A magnetoelastic sensor (shown here is the varying feature density design) is integrated with a biliary stent (partially cut away in this figure to aid visualization of the sensor). External circuitry drives the external interrogation coils to wirelessly measure the response of the implanted sensor. The distributed SrFe permanent magnet layer on the stent biases the magnetoelastic sensor for optimal signal, and does not hinder the stent mechanical operation. As sludge accumulates the frequency response of the sensor changes in a correlated manner.

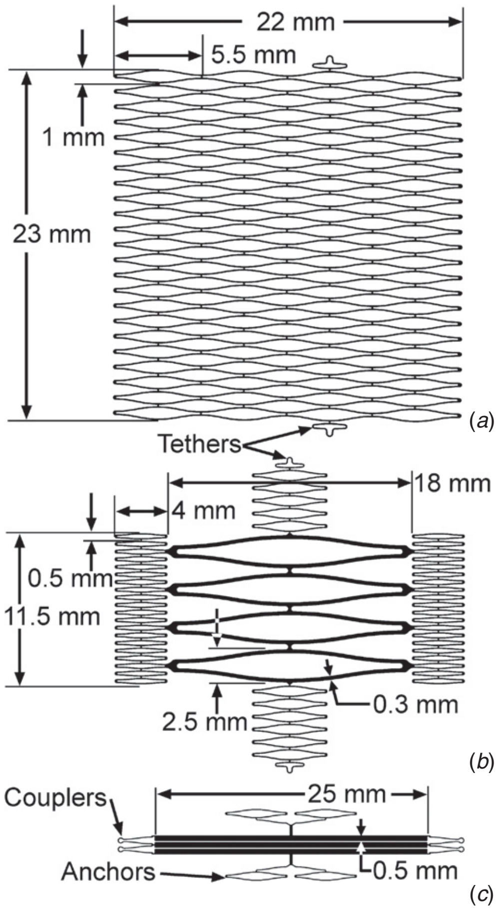

Figure 2. Sensor design layout and important dimensions. (*a*) Spatially sensitive design. (*b*) Varying feature density design. (*c*) Hybrid ribbon design.

method of diagnosis would enable timely intervention and eliminate unnecessary procedures. The method outlined in figure 1 highlights an integrated system providing just such a direct measurement of sludge accumulation in a biliary stent. A magnetoelastic sensor integrated with the stent is caused to resonate by an externally generated ac magnetic field. The frequency response of the sensor changes as local viscosity increases and as sludge accumulates. The mechanical resonance generates an oscillating magnetic flux that can be measured with an external pick-up coil. The frequency content of the voltage induced on the external pick-up coil—including resonant frequencies and phase shifts—can then be measured by the external circuit and correlated to the local sensor environment. The external circuit also drives the transmit coils in an ac frequency sweep that produces the corresponding magnetic field sweep.

We have previously reported on the basic architecture of the system [4]. The implanted device utilizes a batch-fabricated, self-expanding stent coated with a permanent magnet layer (100 μm thick layer of polydimethylsiloxane with suspended strontium-ferrite (SrFe) particles) that provides a uniform and consistent bias field to the integrated magnetoelastic sensor. The previous sensor design was an open mesh-like pattern with elongated cells. This work focuses on sensor designs with added functionality over the basic sensors described in our previous work. Three specific sensor designs are reported here (figure 2). The first sensor design uses a pattern that resonates at two distinct frequencies, with each resonant frequency corresponding to a distinct modal shape. Because the modal shapes are distinct, each is affected differently by the spatial distribution of loads due to sludge accumulation; this allows monitoring of different locations along the length of the stent. The physician can potentially use this added spatial information to develop a better-informed diagnosis and to aid in targeted therapies. The second sensor design implements a pattern with tailored feature density. The increased feature density at specific locations of the sensor results in a localized increase in surface area. This has two effects: first, the sensor-to-environment coupling is increased; second, the biological components that contribute to sludge accumulation (proteins and bacteria) are likely to congregate in such regions [5–7]. By tailoring the sensor geometry such that these regions of large surface area are located at antinodes of the resonant mode shape, sensor sensitivity is improved. The third sensor design uses three narrow ribbons that serve as resonating elements, coupled at the ends with flexible struts. The flexible struts allow the ribbons to slide over one another when the components are compressed inside the delivery sleeve. This design combines the relatively large signal amplitude and robust longitudinal mode shapes of simple ribbon sensors with the flexibility and expandability of the structures used in the first two designs.

This work also gives added focus to sensor material selection and treatment for enhanced utility in this application. Detailed design considerations for the sensor topologies are first described, followed by fabrication information. Finally, experimental methods and results are presented and discussed.

Table 1. Definition of parameters in equations (1)–(10).

E_{app} = Apparent Young's modulus (Pa)
ν = Fluid kinematic viscosity ($\mathrm{m^2\ s^{-1}}$)
ω = Input signal radial frequency ($\mathrm{rad\ s^{-1}}$)
φ = Shape function (1)
E^*_{sludge} = Sludge complex modulus (Pa)
α = Sensor mass damping factor ($\mathrm{s^{-1}}$)
μ_o = Permeability of free space ($\mathrm{N\ A^{-2}}$)
μ = Fluid dynamic viscosity (Pa s)
m_{eff} = Effective mass ($\mathrm{kg\ m^{-2}}$)
$c_{\mathrm{visc,eff}}$ = Effective viscous damping ($\mathrm{kg\ m^{-2}\ s^{-1}}$)
x, ξ = Longitudinal coordinate on sensor (m)
Q = Quality factor (1)
N = Number of turns in pickup coil
ω_o = Characteristic frequency ($\mathrm{rad\ s^{-1}}$)
w = Sensor width (m)
M_o = Sensor mass (kg)
A = Fitting parameter in equation (10) ($\mathrm{kg\ m^{-2}\ s^{-2}}$)
L_{coil} = Pickup coil half-length (m)
t_{sens} = Sensor thickness (m)
t_{sludge} = Sludge thickness (m)
d = Magnetostrictivity ($\mathrm{m\ A^{-1}}$)
ρ_{sens} = Sensor density ($\mathrm{kg\ m^{-3}}$)
ρ_{fl} = Fluid density ($\mathrm{kg\ m^{-3}}$)
ρ_{sludge} = Sludge density ($\mathrm{kg\ m^{-3}}$)
μ_r = Sensor relative permeability (1)
H = Input field strength ($\mathrm{A\ m^{-1}}$)
k_{eff} = Effective stiffness ($\mathrm{N\ m^{-1}}$)
L = Sensor half-length (m)
ω_r = Damped resonant frequency ($\mathrm{rad\ s^{-1}}$)
$c_{\mathrm{visc,fluid}}$ = Effective viscous damping from fluid ($\mathrm{kg\ m^{-2}\ s^{-1}}$)
f_o = Characteristic frequency (Hz)
Δm = Added mass (kg)
Δf = Half-power bandwidth (Hz)
V = Voltage induced on a pickup coil (V)
B = Fitting parameter in equation (10) ($\mathrm{kg\ m^{-2}\ s^{-2}}$)
u = Local sensor displacement (m)

2. Design, modeling and material selection

2.1. *Material selection and treatment for an implantable sensor in a viscous environment*

Numerous magnetoelastic materials have potential utility in this application, and several amorphous alloys (notably Metglas$^{\mathrm{TM}}$ 2826MB, 2605SA1 and 2605CO) provide desirable magnetic and mechanical properties combined with availability and low cost. The magnetoelastic sensor must provide a usable wireless signal to the external interrogation system even under loading from the dynamic biological environment in which the sensor is deployed. The loads experienced by the sensor will include bile—which may shift in viscosity—and accumulating sludge. Because the signal from the sensor is proportional to the strain developed in the sensor, one of the goals of the design strategy is to maintain the strain in the vibrating sensor even as the biliary environment changes. The required strength of the magnetic biasing field is also a consideration.

To evaluate the robustness of the signal from the various materials in the face of viscosity and mass loads, a simple geometry for the sensor is first considered. In our previous work, the longitudinal displacement of a loaded ribbon sensor, u, driven by a harmonic magnetic field along the sensor length was described near the first resonant frequency as

$$u(x,\omega,t) = -\frac{E_{\mathrm{app}}\,\mathrm{d}t_{\mathrm{sens}}H\,\frac{2}{L}\left[\int_0^L \frac{\mathrm{d}\varphi}{\mathrm{d}\xi}\sin\left(\frac{\pi\xi}{2L}\right)\mathrm{d}\xi\right]\mathrm{e}^{\mathrm{i}\omega t}}{\left(\frac{\pi}{2L}\right)^2 k_{\mathrm{eff}} - \omega^2(m_{\mathrm{eff}}) + \mathrm{i}\omega c_{\mathrm{visc,eff}}} \times \sin\left(\frac{\pi x}{2L}\right) \qquad (1)$$

where

$$k_{\mathrm{eff}} = \left(E_{\mathrm{app}} - \frac{E_{\mathrm{app}}^2 d^2}{\mu_o\mu_r}\right)t_{\mathrm{sens}} + 2E^*_{\mathrm{sludge}}t_{\mathrm{sludge}}, \qquad (2)$$

$$m_{\mathrm{eff}} = \rho_{\mathrm{sens}}t_{\mathrm{sens}} + \frac{1}{2}\rho_{fl}\sqrt{\frac{2\nu}{\omega}} + 2\rho_{\mathrm{sludge}}t_{\mathrm{sludge}}, \qquad (3)$$

$$c_{\mathrm{visc,eff}} = 2\mu\sqrt{\frac{\omega}{2\nu}} + \alpha\rho_{\mathrm{sens}}t_{\mathrm{sens}}, \qquad (4)$$

and L is the half-length of the sensor, while x (and the dummy variable ξ substituted in the integral in equation (1)) is the longitudinal coordinate measured from the mid-length of the sensor. The other parameters are defined in table 1. Equation (1) is simplified from that given in [4] by assigning all structural damping in the sensor to the factor proportional to sensor mass in equation (4). Following a treatment in [8], the amplitude of the voltage that is induced on a pickup coil is determined to be proportional to the amplitude of the longitudinal displacement. Assuming that the damping and mass loading due to the fluid medium in which the sensor is immersed is only significant near resonance (so that the frequency at which u is maximum, ω_r, can be substituted for ω in equations (3) and (4)), and substituting the relation for the quality factor

$$Q = \frac{\sqrt{\left(\frac{\pi}{2L}\right)^2 k_{\mathrm{eff}}m_{\mathrm{eff}}}}{c_{\mathrm{visc,eff}}}, \qquad (5)$$

the ratio of the loaded maximum displacement to the unloaded maximum displacement can be expressed as

$$\frac{|u_{\mathrm{max,loaded}}|}{|u_{\mathrm{max,unloaded}}|} \approx \frac{Q_{\mathrm{loaded}}}{Q_{\mathrm{unloaded}}} \approx \frac{c_{\mathrm{visc,eff,unloaded}}}{c_{\mathrm{visc,eff,loaded}}} = \frac{c_{\mathrm{visc,eff,unloaded}}}{c_{\mathrm{visc,eff,unloaded}} + c_{\mathrm{visc,fluid}}}. \qquad (6)$$

This assumes that the mass loading effects of the viscous fluid are small—a valid assumption at frequencies above a few kilohertz. It can be seen in (6) that, in order to maintain signal strength even while immersed in a viscous fluid, the unloaded effective damping of the sensor should be comparable to the damping added by the viscous fluid. With a similar argument, it can be shown that viscoelastic mass loads with a significant damping factor (such as biofilms like sludge [9]) can reduce the loaded amplitude even further. This analysis shows that the sensor material and geometry for this application should provide a large signal while unloaded and also exhibit damping that suitably matches the viscous loads present in the application.

Using a material and geometry with a relatively low quality factor, as is proposed with the above analysis, is

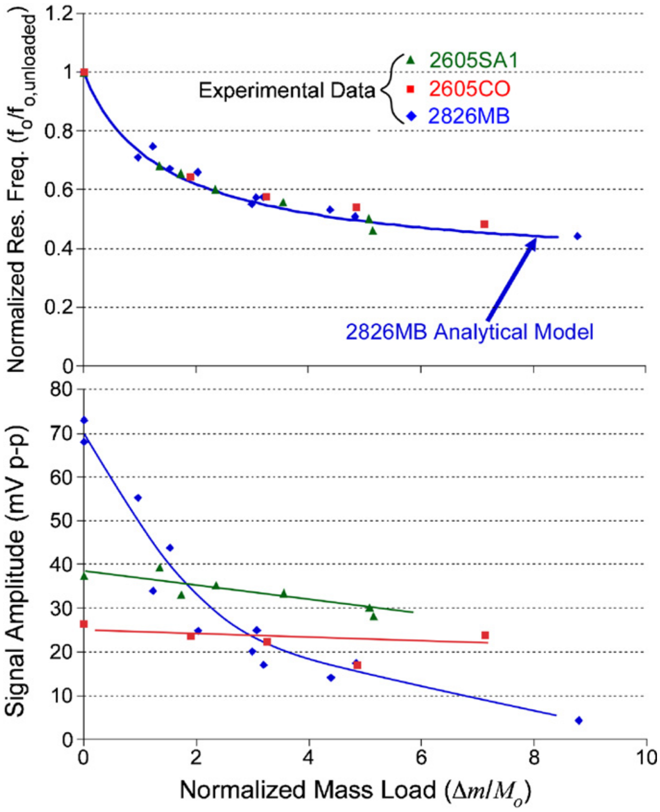

Figure 3. The response of ribbon sensors (2 mm × 37.5 mm) of different alloys to paraffin mass loads. Alternative amorphous metal materials provide similar resonant frequency sensitivity to paraffin mass loads but vastly different amplitude responses due to the differing structural damping of each material. Curves in the bottom graph are guides to the eye.

counter to the design philosophy used in most resonant sensors. Conventionally, a high quality factor is associated with a sharper resonant peak, and thus a smaller minimum resolvable resonant frequency change. Along with the sensitivity of the sensor, this determines the minimum resolvable added mass. However, in contrast with many mass-sensitive resonant sensor applications, in which small amounts of mass accumulate at one binding location in an air or vacuum environment, this application requires measuring a large amount of mass that accumulates everywhere in a liquid environment. As such, the viscoelastic properties of the mass load and the viscous properties of the liquid environment dominate the quality factor of the resonant system. For this reason, improving the inherent quality factor of the unloaded resonating material is not a major point of emphasis for this application.

To provide experimental verification of the principle described in this section, 2 mm × 37.5 mm × 25 μm ribbon sensors were fabricated (using serial mode micro-electro-discharge machining) from three different Metglas^{TM} materials: 2826MB, 2605CO and 2605SA1. Figure 3 shows the frequency and amplitude response of the sensors when loaded by dip-coated paraffin. The frequency response is normalized to the unloaded resonant frequency for each sensor, and the load is normalized to the unloaded mass of each sensor. The amplitude response is not normalized to show the critical findings of this study; although the 2605CO and 2605SA1 sensors have unloaded amplitudes and quality factors that are smaller than that of the unloaded 2826MB sensor, the amplitudes are much less affected by the load. After an added normalized mass of approximately 2, the 2605SA1 sensor has a larger signal amplitude than a similarly loaded 2826MB sensor. After an added normalized mass of approximately 3, the 2605CO sensor has a larger signal amplitude than a similarly loaded 2826MB sensor. Based on the data trends, the 2605CO material may provide the largest signal of any material at large normalized mass loads. These trends are predicted by the analytical model.

Along with maintaining a usable wireless signal under loading, the sensor and the required magnetic biasing layer must present a low profile (to maintain the open flow channel of the stent) and must not hinder the mechanical operation of the stent (especially radial strength, expandability and bending flexibility). Amorphous alloys can all meet these requirements, as they are thin (∼25 μm), can be located along the sidewall of the stent and can also be patterned such that the sensor expandability matches that of the stent. However, each sensor material does require a different biasing magnetic field for maximum response, so the choice of sensor material affects the necessary thickness and geometry of the magnetic biasing layer. In general, a magnetic layer of minimum thickness is preferable to best meet the requirements. For as-cast materials, the required biasing field for Metglas^{TM} 2826MB is approximately 2.3× higher than that required for Metglas^{TM} 2605CO, while the biasing field for Metglas^{TM} 2605SA1 is approximately 1.7× higher than that required for 2605CO. This comparison gives a small advantage to as-cast 2605CO.

To this point in the discussion, only the performance of as-cast material has been considered. Past studies of the magnetoelastic properties of amorphous metals often included annealing of the material in a large transverse magnetic field (e.g. [10–14]). In general, this procedure improves the magnetomechanical coupling coefficient, which is a measure of the efficiency of the material in converting between magnetic energy and elastic energy and vice-versa. Transverse field annealing improves the magnetomechanical coupling coefficient by orienting the moments of the magnetic domains such that they are perpendicular to the long axis of the material. This results in nearly pure rotation of the moments when a field is applied along the long axis of the material, rather than any movement of domain walls [15]. The annealing treatments can also refine the domain structure to reduce micro-eddy currents and associated losses [16]. The practical benefits of transverse field annealing for this application thus include an increase in signal amplitude. The uniform alignment of the magnetic moments also reduces the required bias field.

In order to assist with the material selection, a preliminary evaluation was performed for each of the Metglas^{TM} alloys (2826MB, 2605SA1 and 2605CO) with simple sensor designs. Ribbon-shaped sensors (2 mm × 37.5 mm × 25 μm) were electro-discharge machined from as-cast foils. Each sensor was then placed in a ∼1.5 kOe (120 kA m^{-1}) transverse magnetic field provided between the poles of an AlNiCo

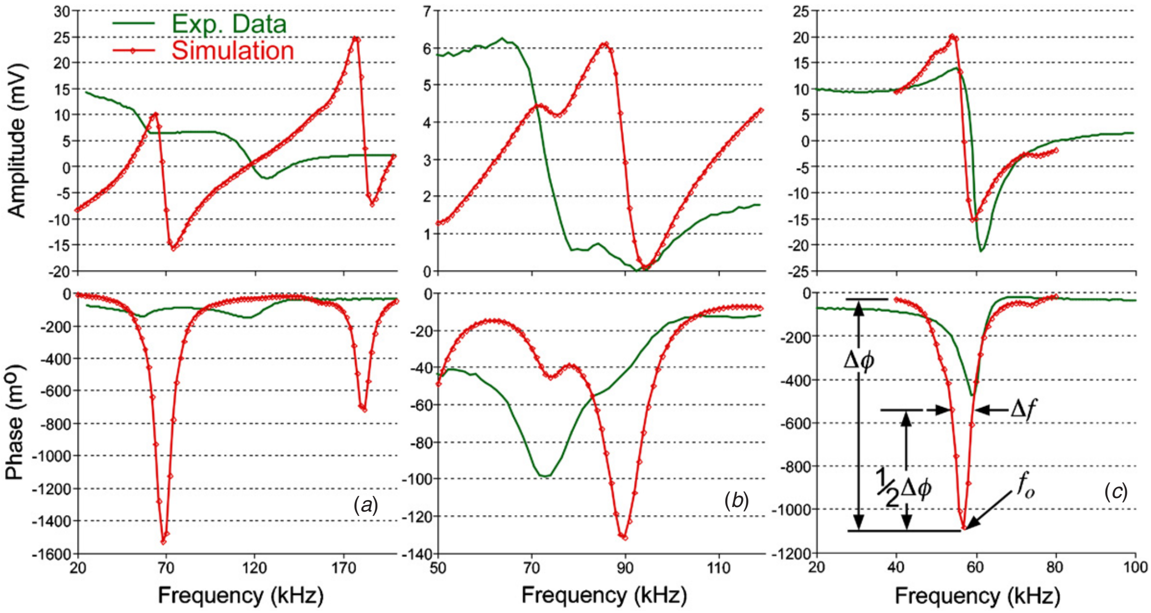

Figure 4. FEA simulated and experimentally measured data. (*a*) Spatially sensitive design. Note that the sensor produces two well-separated resonant responses. (*b*) Varying feature density design. (*c*) Hybrid ribbon design. In the phase chart, the half-power bandwidth and the characteristic frequency of the phase dip are labeled. These parameters are used throughout the results presented in this work.

major magnet and heated above the Curie temperature for the material (353 °C for 2826MB, 395 °C for 2605SA1 and 415 °C for 2605CO). The sensor was held at this temperature for 30 min and removed from the field once cooled to room temperature. The frequency response of the sensor in air before and after the treatment was compared. For 2826MB, the maximum signal amplitude increased by about 10–20% after treatment, while the required bias field was reduced from 4.75 Oe (378 A m^{-1}) to 2.25 Oe (179 A m^{-1}). For 2605SA1, the maximum signal amplitude increased by about 3×, while the required bias field was reduced from 3.75 Oe (298.4 A m^{-1}) to 2 Oe (159.2 A m^{-1}). For 2605CO, the maximum signal amplitude increased by about 3×, while the required bias field increased from 2 Oe (159.2 A m^{-1}) to 7.5 Oe (596.8 A m^{-1}). The increase in required bias field for the 2605CO material may be indicative of non-optimal annealing temperature or transverse field strength. Further exploration of the transverse annealing process, including the effect of annealing time and the performance benefits for more complicated sensor geometry, is presented in section 3 of this work.

Discriminating between the as-cast and transversely annealed Metglas$^{\mathrm{TM}}$ materials in light of the above analysis and the requirements of this application, this paper focuses on transversely annealed sensors fashioned from Metglas$^{\mathrm{TM}}$ 2605SA1. The preliminary tests with ribbon sensors of this material show the best combination of large unloaded signal amplitude, structural damping that best matches the expected damping of viscous bile and viscoelastic sludge, and a low required biasing field. The results in the remainder of this paper illustrate the performance of the treated material in more complex sensor geometries.

2.2. Geometry

This section describes the general concepts for each of the three sensor designs, highlighting specific features that provide the desired functionality. The magnetomechanically coupled finite element analysis (FEA) tool presented in [4] is used to estimate frequency responses, mode shapes and expected signal amplitudes of the sensors. The material properties used in the model are based on available literature values, modified slightly to improve the fit with experimental frequency responses obtained from ribbon sensors fabricated from the actual material used. The predicted responses are shown for each sensor in figure 4.

Design 1: Spatially sensitive sensor. The first sensor design uses a wishbone-array pattern that is similar to the pattern used in sensors presented previously [4]. However, the dimensions of each cell in the pattern and the overall active area of the sensor (figure 2(*a*)) have been modified to provide two advantages. First, the cell has been elongated to result in more expandability. Second, the elongated cell and the wider yet shorter active area results in a tailored frequency response that allows for spatially sensitive monitoring. As shown in figures 4 and 5, the sensor resonates at two distinct frequencies (near 50 kHz and 110 kHz when unloaded, although predicted at 64 kHz and 177 kHz, respectively), with each resonant frequency corresponding to a distinct mode shape. The first mode shape—corresponding to the lower resonant frequency—is mainly longitudinal in nature and produces longitudinal movement of the ends of the active area of the sensor. Meanwhile, the cells in the mid-length of the active area open and close in a transverse motion. In contrast, the second mode shape—corresponding to the higher frequency—shows relatively little movement of the sensor ends, while still

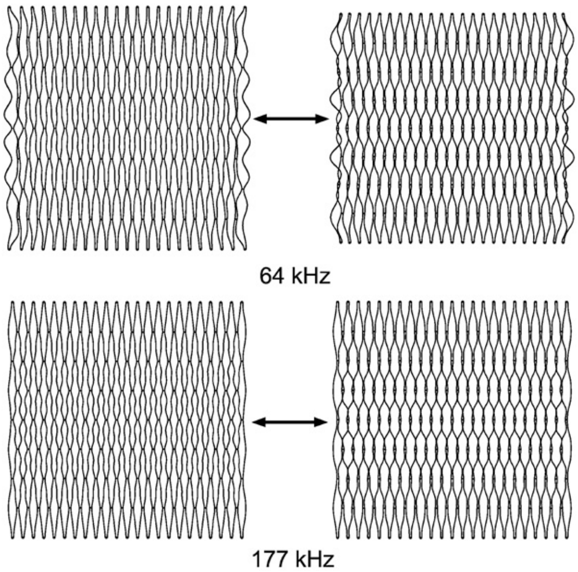

Figure 5. FEA-simulated mode shapes for the spatially sensitive design, along with predicted resonant frequencies. The first mode shape (top) produces extension and contraction of the sensor along the longitudinal (vertical, in this figure) direction, while the second mode shape (bottom) results in little length change but large transverse (horizontal, in this figure) movement of the struts at the middle of the sensor.

showing transverse movement in the cells near the mid-length of the sensor. The spatial arrangement of the nodal and anti-nodal regions of each mode shape determines the sensitivity of the frequency response (i.e. resonant frequency, characteristic damping) of each mode shape to the spatial distribution of sludge. For instance, the presence of sludge at the ends of the active area will act mainly as a mass load on the anti-nodal regions of the first mode shape while acting as a slight stiffening and damping load on nodal regions of the second mode shape. Thus, the lower resonant frequency will shift down, while the higher resonant frequency will shift up slightly (due to increased effective stiffness) or will exhibit a lower quality factor (due to increased damping). Alternatively, the presence of sludge at the middle of the active area will lead to an increase in the first mode resonant frequency (due to increased effective stiffness) or a decrease in quality factor (due to increased damping). The presence of sludge at the middle of the active area is expected to have a more complex effect on the frequency response characteristics, depending on the nature of and distribution of the load. For instance, sludge that has not bridged the interstices of the wishbone-array cells will act primarily as a mass load, lowering the resonant frequency of the mode shape. In contrast, sludge that has bridged the interstices of the wishbone cells may significantly stiffen the structure or add significant damping, resulting in an increase in resonant frequency or a decrease in quality factor, respectively.

Based on the dimensions of the pattern and the mode shapes of each frequency, this sensor is expected to resolve the location of sludge accumulation within about 5 mm along the length of the stent. This added functionality can lead to two benefits for the physician. First, the effects of non-uniform accumulation of sludge will no longer be averaged over the entire active area. This gives the physician better information about the local severity of the disease. Secondly, the doctor can better direct any therapeutic efforts that require such spatial information—e.g. ultrasonic lithotripsy or targeted drug delivery.

Design 2: Varying feature density sensor. While design 1 utilizes a repeated cell throughout the active area, design 2 exploits varying cell size for improving the sensitivity by allowing sludge producing bacteria to preferentially congregate at predetermined locations. These locations, the antinodes of the resonant mode shape, are more sensitive to loading than the remainder of the structure. As shown in figure 2(*b*), larger cells are used in the middle of the active area, while much smaller cells are used at the ends of the active area. This design results in a resonant mode shape that uses the larger features in the middle of the sensor to drive the movement of the smaller features at the ends of the sensor. Thus, the antinodal locations are specifically given a large effective surface area.

In this specific application, an increase in surface area and the presence of fine features may also lead to another favorable result: according to several studies, the biological components that contribute to sludge accumulation (proteins and bacteria) will tend to congregate in such regions [5–7]. The increased surface area—especially of surfaces that are normal to the direction of oscillation—may increase sensor-to-environment coupling through the generation of compressional waves. Compressional waves are a contrast to the shear waves that are generated from the sensor surfaces that are parallel to the direction of oscillation; the effect of shear waves tends to decay quickly in materials that do not support shear stress well, including liquids (such as bile) and biofilms with relatively low rigidity (such as sludge).

Design 3: Hybrid ribbon sensor. As shown in figure 2(*c*), the hybrid sensor design uses three parallel narrow ribbons that are connected at the ends with flexible linkages. The flexible linkages allow the ribbons to slide over one another when the components (stent and sensor) are compressed inside the delivery sleeve; upon removal of the delivery sleeve, the linkages elastically return to their fabricated shape and hold the ribbons apart. Because the linkages are located at the antinodes of the individual ribbons, they also serve to couple the vibrations of the ribbons and enhance the response of the sensor; i.e. the signal amplitude from three coupled ribbons is three times larger than that from a single ribbon. The linkages thus provide the hybrid ribbon sensor with the advantages that are typical of wishbone-array sensors, namely maintaining expandability while allowing an increase in the amount of magnetoelastic material (and associated improvements in signal strength).

The ribbons in the hybrid sensor vibrate in a simple bulk longitudinal mode. This mode shape is advantageous for this application relative to the complicated modes excited in a wishbone-array sensor for two main reasons. First, the longitudinal mode shape is coupled with the transmitted magnetic field more strongly, which is directed primarily longitudinally. Second, the longitudinal mode shape is more robust against the mass, stiffness and damping loads presented by the accumulation of sludge in the interstices of the sensor. In contrast, the bending that takes place in the struts in the mode shapes of a wishbone-array sensor is heavily affected by any interstitial material. Thus, the design of the hybrid sensor combines the favorable mode shapes of ribbon sensors with the desirable expandability of the wishbone-array sensors.

Lateral features are included in each sensor design to facilitate mounting of the sensor to the inner sidewall of the stent. In designs 1 and 2, the spatially sensitive and varying feature density designs, tethers (as shown in figures 2(*a*) and (*b*)) can be woven into the stent structure using any of the braided wires that make up the most commonly used commercial stent design (Boston Scientific Wallstent$^{\text{TM}}$). Alternatively, with stent designs that are patterned from a single piece of metal, integrated mounting features can be included in the stent pattern for weaving into the sensor tethers. In design 3, the hybrid ribbon design, anchors are connected to the active sensor area with struts (see figure 2(*c*)).

2.3. Separation of viscosity and mass response

Monitoring of the environment within the stent would ideally include the ability to separately determine mass accumulation and fluid viscosity changes using the frequency response of the sensor. The resonant frequency of the system has an inverse relationship with mass, while the quality factor has a direct relationship with mass. Thus, simultaneously monitoring the resonant frequency and quality factor of the system can provide the ability to separate the accumulation of mass from changes in viscosity. For a simple second-order resonant system, the quality factor can be determined by dividing the half-power bandwidth of the resonant peak into the resonant frequency. However, this method is made more difficult for the measured wireless amplitude response of a magnetoelastic sensor due to the nearby presence of an anti-resonant frequency that distorts the shape of the resonant peak. Fortunately, the measured separation between the resonant and anti-resonant frequency is also determined by the quality factor of the system, so this more easily measured value can be used as a substitute. To complicate matters further, the exact location of the resonant and anti-resonant frequencies is often difficult to determine for a loaded sensor because the damping added by the load smears the resonant and anti-resonant peaks. However, these difficulties can often be avoided by using the phase response of the sensor, which exhibits a characteristic trough (inverted peak) as illustrated in the hybrid ribbon response shown in figure 4. The shape (i.e. half-power bandwidth, Δf) and location (i.e. frequency at the minimum phase response, f_o) of this phase trough are related to the quality factor and resonant frequency of the system, and as such can be used in combination to separate mass loads from changes in viscosity as described presently.

Further insight into the separation of the effect of mass loads from that of viscosity changes using these measured parameters can be gained by once again investigating the analytical model for the ribbon sensor. Following a treatment in [8], the voltage induced on a pickup coil wrapped perfectly around the ribbon sensor can be described as

$$V(t) = L_{\text{coil}} N \mathrm{i}\omega w \frac{16}{\pi^2} H \mu_0 \mu_r \left[\int_0^L \frac{\mathrm{d}\varphi}{\mathrm{d}x} \sin\left(\frac{\pi x}{2L}\right) \mathrm{d}x \right] \mathrm{e}^{\mathrm{i}\omega t}$$
$$\times \frac{\left(\frac{\pi}{2L}\right)^2 (k_{\text{eff},B}) - \omega^2 (m_{\text{eff}}) + \mathrm{i}\omega c_{\text{visc,eff}}}{\left(\frac{\pi}{2L}\right)^2 (k_{\text{eff}}) - \omega^2 (m_{\text{eff}}) + \mathrm{i}\omega c_{\text{visc,eff}}}, \qquad (7)$$

where

$$k_{\text{eff},B} = E_{\text{app}} t_{\text{sens}} + 2E^*_{\text{sludge}} t_{\text{sludge}}, \qquad (8)$$

N is the number of turns in the pickup coil, L_{coil} is the axial half-length of the pickup coil and w is the width of the sensor. Equation (7) is simplified by making the following assumptions: the damping due to structural hysteresis in the sensor is negligible compared to damping due to the loading material and due to the viscous medium, such that the term containing α in (4) disappears; mass loading due to the viscous medium is negligible compared to other effective mass loads present, such that the second term in (3) disappears; damping due to viscosity is only important near resonance and anti-resonance, allowing the center frequency ω_o to be substituted for ω in (3) and (4); and the real part of the complex sludge modulus is negligible compared to the sensor modulus. After these simplifications, the phase of the voltage can be analyzed to find the frequencies at which the phase is −180° (the resonant and anti-resonant frequencies, separated by Δf) and at which the phase is at its minimum (the characteristic frequency, f_o). With rearrangement, the added mass (Δm) can be written in terms of the characteristic frequency, f_o, as follows:

$$\frac{\Delta m}{M_o} = \left(\frac{f_{o,\text{unloaded}}}{f_o}\right)^2 - 1, \qquad (9)$$

where M_o is the mass of the sensor and $f_{o,\text{unloaded}}$ is the frequency at which the minimum phase occurs for an otherwise unloaded sensor. The result of (9), along with the expression of the resonant and anti-resonant frequency separation (Δf), can be used to write the viscosity–density product of the fluid medium in terms of Δf and f_o. To leading order

$$\mu\sqrt{\frac{1}{\nu}} = \sqrt{\mu\rho_{fl}} = A\frac{\Delta f}{f_o^{\frac{5}{2}}} + B\frac{1}{f_o^{\frac{3}{2}}}, \qquad (10)$$

where A and B are constants dependent on sludge and sensor material properties. A and B can be used as fitting parameters for use in sensor calibration, as is done in the remainder of this work.

3. Fabrication

The sensors are batch patterned from a 25 μm thick foil of as-cast 2605SA1 Metglas$^{\text{TM}}$ utilizing a photochemical machining (PCM) process [4, 17]. Feature sizes of the individual struts are 100 μm. Other important dimensions are shown in figure 2.

To improve the signal amplitude, the sensors are thermally treated in a large transverse magnetic field. Sensors are layered in between glass slides that are held together with an Elgiloy$^{\mathrm{TM}}$ (Cr-Ni, non-magnetic) retaining spring. This stack is then placed in a ∼1.5 kOe (120 kA m^{-1}) magnetic field provided in the 3.75 cm wide gap of an AlNiCo major magnet, with the field directed transverse to the long axis of the sensor. The stack is then heated above the Curie temperature for 2605SA1 (395 °C) and held at temperature (413 °C). With a 3 h treatment, the signal amplitude for the spatially sensitive design improves by an average of 5×, the signal amplitude for the varying feature density design improves by an average of 4× and the signal amplitude for the hybrid ribbon design improves by an average of 15×. The average amplitude improvement as a result of the transverse field annealing process is dependent on sensor design. This dependence may be a result of feature size or feature density affecting the ability of the transverse field to penetrate the sensor material, or it may be a result of the more transverse mode shapes in the spatially sensitive and varying feature density designs being less improved by the reorientation of magnetic domains. The number of sensors in the annealing stack does not significantly affect the treatment outcome, as long as the sensors remain in between the poles of the magnet. Additionally, the permeability of the material used to sandwich the sensors has little effect on the outcome.

The stent application calls for a generally tubular shape, so the sensor must be curved into a tubular or semi-tubular shape to best match the stent geometry. Initial attempts to add curvature to the sensor via elastic bending (e.g. by rolling the sensor and stent into a tube) resulted in a resonant frequency shift and a severe decrease in the amplitude of the sensor signal. This effect is thought to be the result of a combination of mechanical stress imposed in the material, as well as geometrical changes in the mode shapes. The tubular shape is achieved in this work by placing the sensor against the inner wall of a metal tube and annealing at 375 °C. By annealing the sensor in the curved state, mechanical stress in the material is relieved while the desired shape is maintained, leaving only geometrical changes in the mode shapes to affect the sensor response. These changes are less significant than those imposed by mechanical stress, especially if the design anticipates the curvature (e.g. by using FEA models that incorporate curved designs). This thermal treatment is applied to the sensor below the Curie temperature of the material in order to retain the signal amplitude gain resulting from the previous treatment in the transverse magnetic field. The amount of springback that occurs after this treatment varies for each sensor design as a result of the different bending stiffness of each design. Therefore, the diameter of the metal tube and the annealing time must be chosen for each design to achieve the desired final curvature. As an example, a 6 h treatment in a 5 mm diameter tube results in a 9 mm final curved diameter for the spatially sensitive and varying feature density designs. For the hybrid ribbon design, a 1.5 h treatment in a 2.3 mm diameter tube results in a 7 mm final curved diameter.

The iron content in the amorphous alloys can result in a tendency for the material to corrode in aqueous environments, shifting and diminishing the sensor response. To passivate the material, the sensors are coated in a conformal layer of 2 μm thick Parylene-C (polyxylylene) using a standard vacuum deposition technique. This process results in minimal shifts in the frequency response and amplitude of the sensors. The coating process should be done subsequent to the thermal processes described above, as the polymer coating is susceptible to degradation at the high temperatures involved in those processes. After this process, the sensors are notably more robust in corrosive environments.

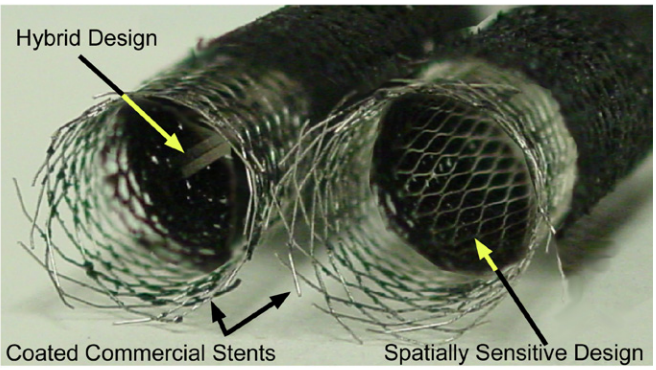

Figure 6. Sensors integrated with commercial self-expanding biliary stents (8 mm diameter × 60 mm length, Boston Scientific Wallstent$^{\mathrm{TM}}$). The sensor anchors are bonded to the stent with PDMS.

The sensors can be bonded to stents using the anchors or tethers built into the design. A number of attachment methods can be used: a thin layer of PDMS (as used in this work) or other biocompatible adhesive, with a parylene–parylene bond [18] or with welding. Note that either of the mounting features described in section 2 (i.e. tethers or anchors) is interchangeable among the sensor designs. Examples of spatially sensitive and hybrid ribbon designs integrated with a commercial stent that has been coated with a conformal magnetic biasing layer are shown in figure 6.

4. Experimental methods

Isolated sensors (i.e. not attached to stents) were tested unless otherwise noted. The mounting processes were verified experimentally to have no significant effect on the sensor response. Magnetic biasing of the sensors was applied through the use of dual Helmholtz coils. The coaxial configuration (described in [4]) was used for interrogation of the sensors for all test results reported here.

Paraffin was used as a sludge simulant. For designs 2 and 3, the varying feature density and hybrid ribbon designs, the entire sensor was immersed in the melted paraffin and then removed to build up successive layers. For design 1, the spatially sensitive design, this process was modified slightly to better control the spatial distribution of the paraffin so that effects on each mode shape could be separately characterized. The paraffin was added to the ends of the spatially sensitive sensor by dipping only the ends of the sensor into the melted paraffin, one end at a time. To add paraffin to the middle of the sensor, melted paraffin was placed in a pipette and drizzled onto the desired location before solidification occurred.

Before and after adding mass to the sensors, measurements were taken with the sensors immersed in fluids of various known viscosities (air; DI water; Dow Corning 200 2, 5, 10 and 20 cS fluids). This procedure allowed for further experimental investigation into the separation of mass and viscosity effects, a procedure described in section 2. After immersion and measurement in fluid, the sensor was cleaned and paraffin reapplied before further testing. To investigate the effect of sludge material properties on the response of the sensor, an alternative method for simulating sludge was also used. With this method, the sensors were first separately positioned inside 6–8 mm diameter plastic tubes; the diameter of the tube used matched the diameter of the curved sensor. Subsequently, the sensors and tubes were immersed in a gelatin–water mixture (1/2 oz of unflavored gelatin powder fully dissolved in 144 mL of deionized water). The mixture was allowed to fully cure (via refrigeration for 6 h), and then the sensors and tubes were removed. At this point, the tubes were completely filled with cured gelatin, and the sensors were completely encased along the sidewall of the tube. After allowing the gelatin to reach room temperature (∼15 min), the response of each sensor was measured. Then a thin-walled metal tube was used to core out a channel in the gelatin near the center axis of each tube. Again, the sensor response was measured. Subsequently, larger diameter channels were cored out of the gelatin followed by measurement of the sensor response. This procedure allowed the response of each sensor to be correlated to a patent diameter, with the gelatin remaining at each step representing the occluding sludge. For this portion of the testing, the sensors (and tubes and gelatin) were not immersed in liquids because of the concern that liquids might change the gelatin properties and result in a poorly controlled test.

5. Experimental results

The experimentally measured responses for the unloaded sensors are compared with the predicted responses in figure 4. The match between the FEA-predicted response and the experimentally measured response becomes worse as the main features of the vibrating pattern become smaller. In particular, the match in figure 4(*a*) (the spatially sensitive sensor, which has 100 μm thick struts) is worse than the match in figure 4(*c*) (the hybrid ribbon sensor, which has 500 μm thick ribbons). This indicates that feature size may have a significant effect on the benefits of transverse field annealing and critical material properties.

Figure 7 shows the measured signal from design 3, the hybrid ribbon sensor, after passing through each of the process steps described in section 3: photochemical machining, transverse field annealing, thermal curvature addition and parylene coating. The shifts in amplitude and frequency response for each step are similar for the other two designs (although the magnitude of the amplitude change after transverse field annealing for the other designs is smaller, as noted previously).

Figure 8 shows the results for paraffin loading of design 1, the spatially sensitive sensor. As can be seen, each of the characteristic frequencies responds differently to the presence of paraffin in the two locations (ends of the sensor, middle of the sensor). Note that the characteristic frequency of the second mode tends to increase when paraffin is placed on either location, albeit with a different sensitivity for the two locations. This indicates that the paraffin tends to add stiffness to the vibration of the second mode shape, likely by bridging the interstices of the pattern. This trend is also seen in the characteristic frequency of the first mode when mass is added to the middle of the pattern.

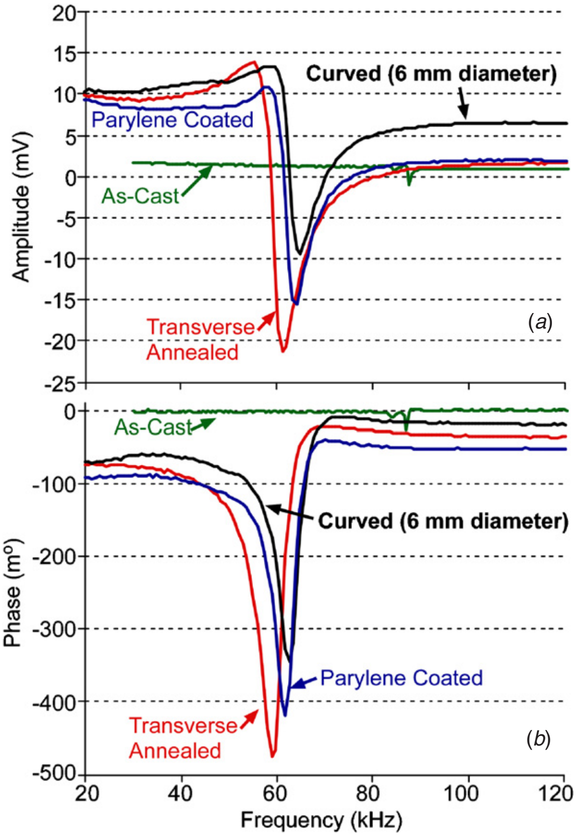

Figure 7. Changes in sensor amplitude (*a*) and phase (*b*) response after the listed treatments applied to the hybrid ribbon design. Note that the transverse field annealing step produces a huge change in the amplitude and phase response. Changes due to parylene coating and addition of curvature are similar in magnitude and much smaller than the changes due to transverse field annealing.

The response of the two characteristic frequencies can be used to separately characterize the amount of paraffin in each location using only the measured characteristic frequencies. First, the equations for each characteristic frequency in figure 8 are superposed, then $\Delta m_{\mathrm{end}}/M_o$ and $\Delta m_{\mathrm{mid}}/M_o$ are determined in terms of $f_{o,L}$ and $f_{o,H}$. The resulting relationships can be used to estimate the amount of mass at each portion of the stent. As shown in table 2, the mass added in each location is calculated using this method and compares well with the actual added mass. Further characterization and empirical modeling may improve the ability to estimate the distribution of the mass loads.

Figure 9 shows the results for paraffin loading of design 2, the varying feature density sensor, along with a curve representing a typical response for the sensor designs described in [4]. Note that, compared to previous designs, the resonant frequency of the sensor is much more sensitive to the addition of mass throughout this range. Additionally,

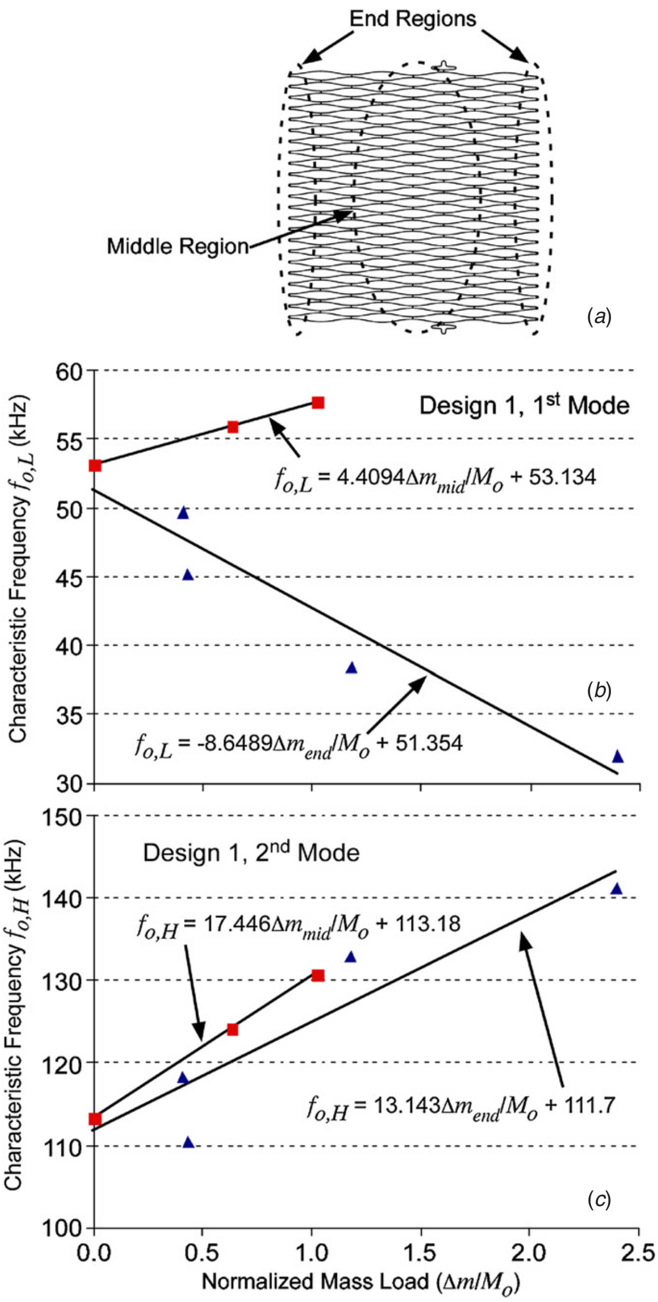

Figure 8. Paraffin loading results for design 1, the spatially sensitive sensor. The top sketch (*a*) illustrates the locations where paraffin is applied for the 'mid' and 'end' responses. Chart (*b*) shows that the characteristic frequency of the first mode decreases as mass is added to the end, while the characteristic frequency increases as mass is added to the mid-length. Chart (*c*) shows that the characteristic frequency of the second mode increases for mass added at both locations, with a slightly different rate for each location.

Table 2. Calculated mass distribution using measured characteristic frequencies.

		Actual		Calculated	
$f_{o,L}$ (kHz)	$f_{o,H}$ (kHz)	$\Delta m_{\mathrm{end}}/M_o$	$\Delta m_{\mathrm{mid}}/M_o$	$\Delta m_{\mathrm{end}}/M_o$	$\Delta m_{\mathrm{mid}}/M_o$
50.88	125.5	0.4046	0.3817	0.3929	0.4605
45.25	130.75	1.2366	0.3817	0.9732	0.3219
47.5	128.5	0.4275	0.5115	0.7381	0.3709

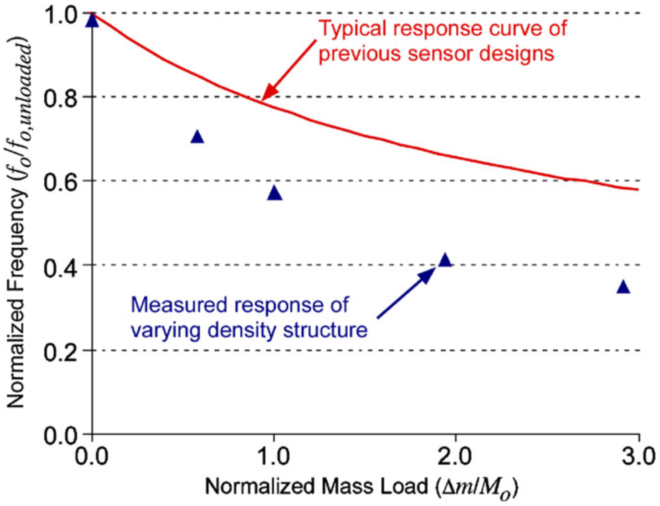

Figure 9. Loading results for design 2, the varying feature density sensor. Note the increased sensitivity as compared to designs presented in [4].

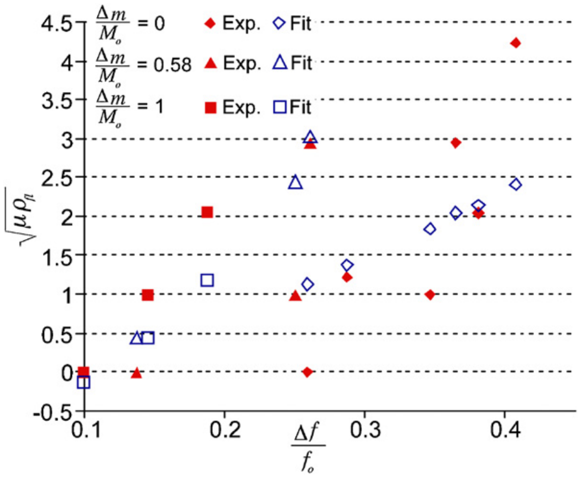

Figure 10. Separation of effects of viscosity from those of paraffin mass loads for design 2, the varying feature density sensor. Although the fitted results do not exactly match the experimental results, the trends are well predicted.

it was observed that, due to meniscus formation across the small features at the ends of the sensor, the paraffin tends to build up in the areas of high feature density (as expected for sludge).

Figure 10 shows the separation of viscosity and mass effects for design 2, the varying feature density sensor, using the procedure described in section 2 (i.e. using equation (10) and fitting parameters *A* and *B* to the data). Although the data are not precisely fitted, general trends are fit well. Further data collection and empirical model fitting may improve the precision of this method.

Figure 11 shows the results for paraffin loading of design 3, the hybrid ribbon sensor. The hybrid ribbon shows slightly worse sensitivity to paraffin loading than ribbon sensor designs discussed in [4]; this may be due to the very different aspect

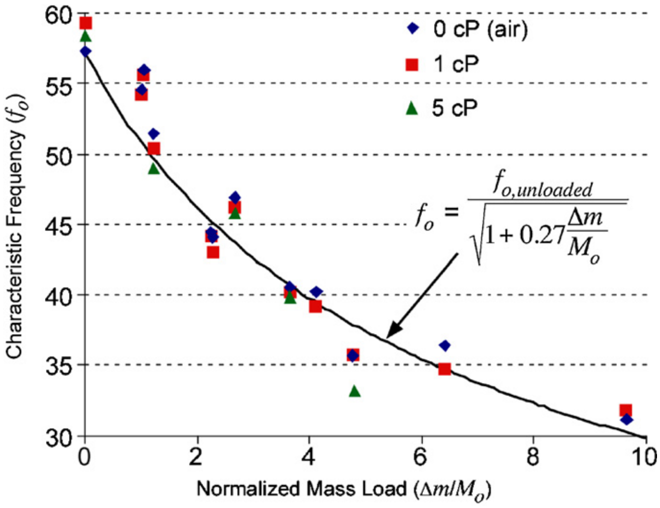

Figure 11. Paraffin loading results for design 3, the hybrid ribbon sensor. Note the minimal effect on characteristic frequency that a change in viscosity produces. The curve is fit to the data points using an equation with the form shown and varying the term multiplying the normalized mass load. The variability in data for similar mass loads is likely attributable to a slightly different (and non-uniform) distribution of mass on the sensor for each mass load.

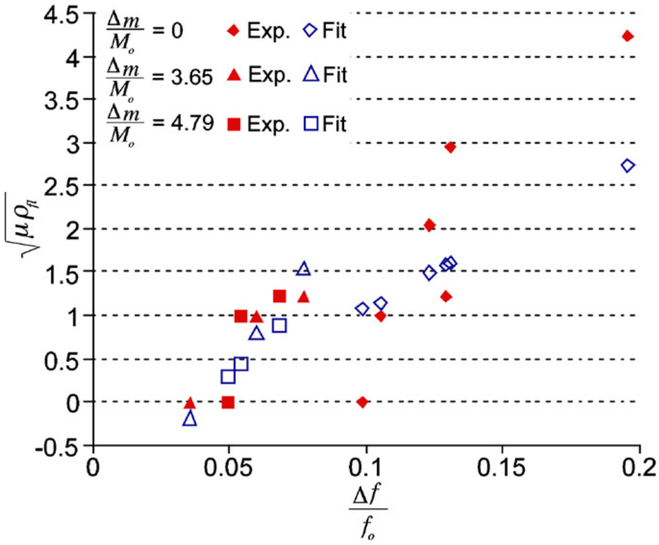

Figure 12. Separation of effects of viscosity from those of paraffin mass loads for design 3, the hybrid ribbon sensor. The results for large mass loads and low viscosities are especially well fit.

ratio of the ribbons used in the hybrid ribbon design compared to previous designs, or it may be different because the paraffin tended to be distributed differently on the sensor due to the small gaps between the ribbons or due to other small features. However, the characteristic frequency response is still fitted well with only a small modification of the relationship suggested by the analytical model for a simple ribbon sensor given in equation (9).

Figure 12 shows the separation of viscosity and mass effects for design 3, the hybrid ribbon sensor. Again, the general trends for viscosity are fit well, and improvement may be possible through further data collection and parameter fitting. In general, design 2, the varying density sensor, is slightly more sensitive to changes in viscosity than the hybrid ribbon sensor, with $\Delta f/f_o$ varying over a wider range as viscosity changes for a given normalized mass load. This larger sensitivity is thought to be an effect of the greater interaction of the small features at the ends of the varying density sensor with the environment.

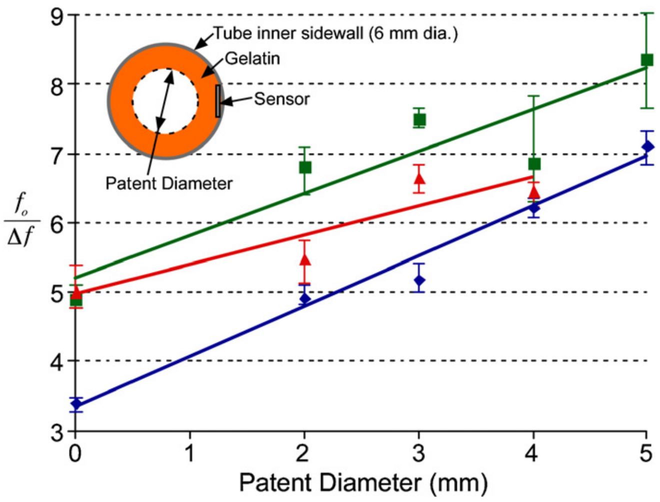

Figure 13. Gelatin loading results for design 3, the hybrid ribbon sensor. Three separate runs using the same sensor are shown, fit with linear regression. Error bars for each data point signify the range of values obtained from three measurements at that point, while the data point signifies the average of the three measurements. Note that, within a test run, the sensor demonstrates a resolution of ~2 mm of patent diameter and remains sensitive until the tube is fully occluded. However, the absolute sensor output shows a large variability from one test run to the next.

Figure 13 shows the results for three trials using gelatin and a hybrid ribbon sensor (within a 6 mm diameter tube). Note that, as the patent diameter increases, $f_o/\Delta f$ increases. These results indicate that, within a given test run, the sensor can resolve the difference between 2 mm of patent diameter and a fully occluded duct, using $f_o/\Delta f$ as the measurand. The trends for the other designs are similar and indicate similar resolution within test runs.

6. Discussion

The spatially sensitive sensor is able to discriminate between accumulation of material at the ends of the sensor and accumulation of material at the middle of the sensor, corresponding to a spatial resolution of about 5 mm along the length of the sensor. The basic concept of using mode shapes with sufficiently different frequency responses (so that each response can be measured separately) and targeted nodal and anti-nodal locations for spatial sensitivity can be applied to many different design architectures. The particular advantage of the open, mesh-like architecture studied here—expandability—is specific to the application in self-expanding biliary stents or in any other application where minimizing the sensor profile prior to deployment is necessary. In fact, spatially sensitive designs mounted in commercially available self-expanding stents survive compression into and redeployment from a 2 mm diameter delivery sleeve, with no significant changes to signal amplitude or frequency response.

As predicted, the varying feature density sensor shows approximately 2× sensitivity increase to both mass loading and viscosity changes over previously described ribbon and wishbone-array sensor designs. One disadvantage of this particular design is low signal amplitude—possibly a result of energy loss in the higher-order bending modes that are induced in the driving sections during resonant vibration.

The hybrid ribbon sensor takes advantage of the coupling efficiency provided by extensional vibration, while still maintaining an open, expandable structure that can be compressed into a delivery configuration for a self-expanding biliary stent monitoring system. For example, a sensor mounted to a commercial stent (Wallstent$^{\mathrm{TM}}$, Boston Scientific) can survive compression into a 2 mm diameter tube. After subsequent expansion, the sensor exhibits negligible changes in amplitude and frequency response. The signal amplitude from this design is high, and the amplitude remains high even when heavily loaded. Though the sensitivity is somewhat lower than other designs, the full-scale range and wireless range of the hybrid ribbon design exceed those of the other complex designs (i.e. wishbone-array [4], spatially sensitive, and varying feature density designs). Sensitivity may be improved by incorporating small features at the ends of the design, as suggested by the results presented for the varying feature density design. Finite element modeling and preliminary experiments suggest that signal amplitude may be further increased by adding more ribbons linked together with flexible couplers.

When sensor performance under gelatin loading is evaluated across different test runs, further insight is gained. Though the sensitivity for each trial is similar, the offset between trials is large. For instance, a measured $f_o/\Delta f$ of 6 indicates a patent diameter of about 1 mm for one test run, while the same measured value indicates a patent diameter of about 4 mm for another test run using the same sensor in the same tube. This behavior suggests that the significant sources of variability exist. One potential source of variability is the slightly different distribution of gelatin around the sensor after coring out a flow channel. Because the mode shape (and thus sensitivity to loads) is distributed spatially, any variation in the spatial distribution of the loads will result in a different sensor response. This variability is also seen with the paraffin testing, but at a much less significant level. Another potential source of variability is the gap between the sidewall and the sensor. Because the sensor is not fixed in the tube, a different gap between the sidewall of the tube and sensor may exist for each run. This can result in a different boundary condition for the sensor, which will affect the response. An additional source of variability may be the material properties of the gelatin due to processing variations. Unfortunately, in the end use of this device, all of these sources of variability are likely to exist: sludge will accumulate with a different distribution each time, sludge components (and hence material properties) will be different in each case, and the sensor may be deployed such that a slightly different gap between the inner duct wall and sensor exists. A target for future designs is to reduce sensitivity to these sources of variability.

Comparing the results of the gelatin testing with results from paraffin testing provides some worthy insight into the operation of resonant sensors when loaded by materials with different viscoelastic properties. In contrast to paraffin loading, the gelatin loading affects the quality factor of the resonance (as measured by $f_o/\Delta f$) more significantly than the characteristic frequency (f_o). The results of this testing indicate that, for a viscoelastic load, the important parameter to measure depends on which regime (viscous or elastic) is more dominant for the loading material in question. The stiffer paraffin tends to have a large effect on the amplitude of the response, especially when it accumulates in the interstices of the sensor pattern. In contrast, the gelatin has a large effect on the quality factor of the sensor response while insignificantly affecting the characteristic frequency. Also, gelatin-filled interstices do not have a major effect on sensor signal amplitude. Actual loading materials encountered in the end-use applications of these sensors may be more gelatin like or more paraffin like, or could have some combination of the viscoelastic properties of the two materials. Regardless of the dominant regime, these tests show that the ability provided by the magnetoelastic sensor to monitor both characteristic frequency and quality factor simultaneously should allow useful information about the load (and more importantly the disease progression) to be determined.

The sensors investigated here used transversely annealed Metglas$^{\mathrm{TM}}$ 2605SA1. As described in section 2, this material was expected to offer increased amplitude robustness while loaded as compared to other Metglas$^{\mathrm{TM}}$ alloys, while still retaining sufficient frequency response sensitivity to the loads. However, one consequence of this material choice is that the sensitivity of the quality factor—which, as found in this work, plays an important role in the measurement of viscosity and viscoelastic damping effects—is lower than it could be with other materials. The transverse field annealing treatment, which lowers the exhibited quality factor of the material (and thus makes it less sensitive to damping), also exacerbates this situation. The degradation in quality factor sensitivity is further compounded by the complex mode shapes of the wishbone-array, spatially sensitive, and varying feature density designs; the bending and transverse movements induced in these mode shapes lead to significant structural damping. Future designs should take into account the need to balance amplitude robustness with sensitivity.

It may be fruitful in future designs to combine each of the concepts that have been demonstrated here into one sensor (or sensor array). For example, the results of the gelatin testing presented in this paper suggest that significant variability may be introduced in the sensor response due to the spatial distribution of the loading material. Hence, it may be best to deploy an array of sensors, each with sensitivity to accumulation only in one spatial location.

7. Conclusion

This paper presents three wireless magnetoelastic sensor designs for use in biliary stent monitoring, each with enhanced functionality due to tailored geometry. The sensors are all batch patterned using photochemical machining, which is a process that provides significant leeway in adding small features (∼100 μm) to relatively large patterns (25–50 mm). A spatially sensitive design uses a wishbone-array repeated pattern with specific overall active area dimensions to provide the ability to separate the spatial location of mass loads with a resolution of about 5 mm along the length of the biliary stent. A varying feature density design uses large features at the mid-length of the pattern and fine features at the ends of the pattern to improve sensitivity to mass loads by a factor of 2. A hybrid ribbon design uses flexible couplers to join narrow ribbons to result in a sensor that combines the flexibility and expandability of the other designs with the robust longitudinal mode shapes of ribbon sensors. Bench-top *in vitro* testing with paraffin and gelatin as biliary sludge simulants shows that the characteristic frequency and half-power bandwidth of the phase response of the sensors can be used to evaluate the viscoelastic loads on the sensors and thus allow real-time monitoring of the continued patency of the biliary stent. Although the specific designs presented here have been developed with self-expanding metal stents in mind, the concepts can be equally applied to designs that are appropriate for non-expanding polymeric stents as well. Many other variations on the ideas presented in this work can also be envisioned, each with potential performance enhancements, but the framework laid here in the form of devices and results is important.

Acknowledgments

The authors acknowledge Professors Grace Elta and Richard Kwon of the Department of Internal Medicine, Division of Gastroenterology for discussions regarding stent usage and desired sensor performance. Dr Mark Richardson assisted with interrogation system design and implementation. Ms Seow Yuen Yee assisted with parylene coating steps. Metglas Inc., Hoosier Magnetics, and Dow Corning provided samples for this project. This work was supported in part by a NSF Graduate Research Fellowship to SG, the NSF ERC for Wireless Integrated Microsystems (WIMS), and the University of Michigan.

References

[1] Donelli G, Guaglianone E, Di Rosa R, Fiocca F and Basoli A 2007 Plastic biliary stent occlusion: factors involved and possible preventive approaches *Clin. Med. Res.* **5** 53–60

[2] Sung J 1995 Bacterial biofilm and clogging of biliary stents *J. Ind. Microbiol.* **15** 152–5

[3] Classen M, Tytgat G and Lightdale C 2002 *Gastroenterological Endoscopy* (Stuttgart: Thieme)

[4] Green S and Gianchandani Y B 2009 Wireless magnetoelastic monitoring of biliary stents *J. Microelectromech. Syst.* **18** 64–78

[5] Coene P, Groen A, Cheng J, Out M, Tytgat G and Huibregtse K 1990 Clogging of biliary endoprostheses: a new perspective *Gut* **31** 913–7

[6] Dowidar N, Kolmos H, Lyon H and Matzen P 1991 Clogging of biliary endoprostheses: a morphologic and bacteriologic study *Scand. J. Gastroenterol.* **26** 1137–44

[7] Dowidar N, Kolmos H and Matzen P 1992 Experimental clogging of biliary endoprostheses. Role of bacteria, endoprosthesis material, and design *Scand. J. Gastroenterol.* **27** 77–80

[8] O'Dell T 1982 Measurement of magnetomechanical coupling factor in amorphous ribbons *Phys. Status Solidi* a **74** 565–72

[9] Cense A, Peeters E, Gottenbos B, Baaijens F, Nuijs A and van Dongen M 2006 Mechanical properties and failure of *Streptococcus mutans* biofilms, studied using a microindentation device *J. Microbiol. Methods* **67** 463–472

[10] Clark A and Wun-Fogle M 1989 A new method of magnetostrictivity and magnetostriction measurement *IEEE Trans. Magn.* **25** 3611–3

[11] Hyoung Kim M, Shik Lee K and Ho Lim S 1999 Magnetostriction measurements of metallic glass ribbon by fiber-optic mach-zehnder interferometry *J. Magn. Magn. Mater.* **191** 107–12

[12] Zhai J, Dong S, Xing Z, Li J and Viehland D 2006 Giant magnetoelectric effect in Metglas/polyvineliden-fluoride laminates *Appl. Phys. Lett.* **89** 083507

[13] Anderson P III 1982 Magnetomechanical coupling, ΔE effect, and permeability in FeSiB and FeNiMoB alloys *J. Appl. Phys.* **53** 8101–3

[14] Modzelewski C, Savage H, Kabacoff L and Clark A 1981 Magnetomechanical coupling and permeability in transversely annealed Metglas 2605 alloys *IEEE Trans. Magn.* **MAG-17** 2837–9

[15] Spano M, Hathaway K and Savage H 1982 Magnetostriction and magnetic anisotropy of field annealed Metglas 2605 alloys via DC M-H loop measurements under stress *J. Appl. Phys.* **53** 2667–9

[16] Herzer G 2003 Magnetic materials for electronic article surveillance *J. Magn. Magn. Mater.* **254–255** 598–602

[17] ASM International 1989 *ASM Handbook* vol 16 (Materials Park, OH: ASM International)

[18] Kim H and Najafi K 2005 Characterization of low-temperature wafer bonding using thin-film parylene *J. Microelectromech. Syst.* **14** 1347–55